OPEN

Correspondence and
requests for materials
should be addressed to
M.G. (mgu@swin.edu.
au)

Breaking the diffraction-limited resolution barrier in fiber-optical two-photon fluorescence endoscopy by an azimuthally-polarized beam

Min Gu, Hong Kang & Xiangping Li

Centre for Micro-Photonics, Faculty of Engineering & Industrial Sciences, Swinburne University of Technology, Hawthorn, Victoria 3122, Australia.

Although fiber-optical two-photon endoscopy has been recognized as a potential high-resolution diagnostic and therapeutic procedure *in vivo*, its resolution is limited by the optical diffraction nature to a few micrometers due to the low numerical aperture of an endoscopic objective. On the other hand, stimulated emission depletion (STED) achieved by a circularly-polarized vortex beam has been used to break the diffraction-limited resolution barrier in a bulky microscope. It has been a challenge to apply the STED principle to a fiber-optical two-photon endoscope as a circular polarization state cannot be maintained due to the birefringence of a fiber. Here, we demonstrate the first fiber-optical STED two-photon endoscope using an azimuthally-polarized beam directly generated from a double-clad fiber. As such, the diffraction-limited resolution barrier of fiber-optical two-photon endoscopy can be broken by a factor of three. Our new accomplishment has paved a robust way for high-resolution *in vivo* biomedical studies.

S ince the invention of two-photon fluorescence microscopy that adopts a high numerical aperture (NA) objective[1,2] to enables three-dimensional (3D) imaging through tissue with image resolution a sub-micrometer scale[1–3], significant progress has been made in developing fiber-optical two-photon endoscopy with a compact probe[4–12]. However, the advance of image resolution in fiber-optical two-photon endoscopy has reached only a few micrometers due to the optical diffraction barrier of a low NA objective. Typically, the image resolution for an endoscope probe with NA = 0.35[6] is approximately 1.75λ (or 1.24λ for two-photon image resolution), which makes it impossible to obtain the sub-wavelength details of organs that can provide valuable information for early diagnosis of diseases and for understanding complex mechanisms of bio-phenomena[4,5,13].

Recently, stimulated emission depletion (STED) microscopy has been demonstrated to be a powerful tool to break far-field resolution barrier[14–18]. In a typical table-top STED microscope[14,16], a Gaussian-shaped excitation focal spot is overlapped with a doughnut-shaped STED focal spot featuring a zero-intensity point at the focal center for the depletion of fluorophores. For a high NA objective in a bulky STED system, a circular doughnut-shaped focal spot can be generated only under the illumination of a circularly-polarized beam superposed with a phase vortex of appropriate handedness and topological charge[14,19,20]. However, this kind of the illumination condition cannot be met through a length of optical fiber because of its birefringence. On the other hand, it has been theoretically predicted that the azimuthally polarized beam with a doughnut shape could be used to perform STED in a table-top microscope[21–25]. In particular, cylindrically polarized beams including azimuthally polarized and radially polarized modes could be directly generated from single-clad fibers[26,27]. Here, we demonstrate for the first time that STED fluorescence imaging can be achieved in the compact fiber-optical endoscopy system with an azimuthally-polarized beam generated from the core of a double-clad fiber (DCF). Our experimental results have demonstrated that the diffraction-limited resolution barrier can be broken by a factor of 3. Consequently, the highest image resolution of 310 nm is achieved for the endoscopic probe of NA = 0.35, which should correspond to the image resolution of 75 nm if the NA was 1.2.

Results

Doughnut focal spot generated by an azimuthally-polarized beam. The zero central intensity, the size and the small full width at half maximum (FWHM) of a doughnut shaped focal spot are three key elements in achieving
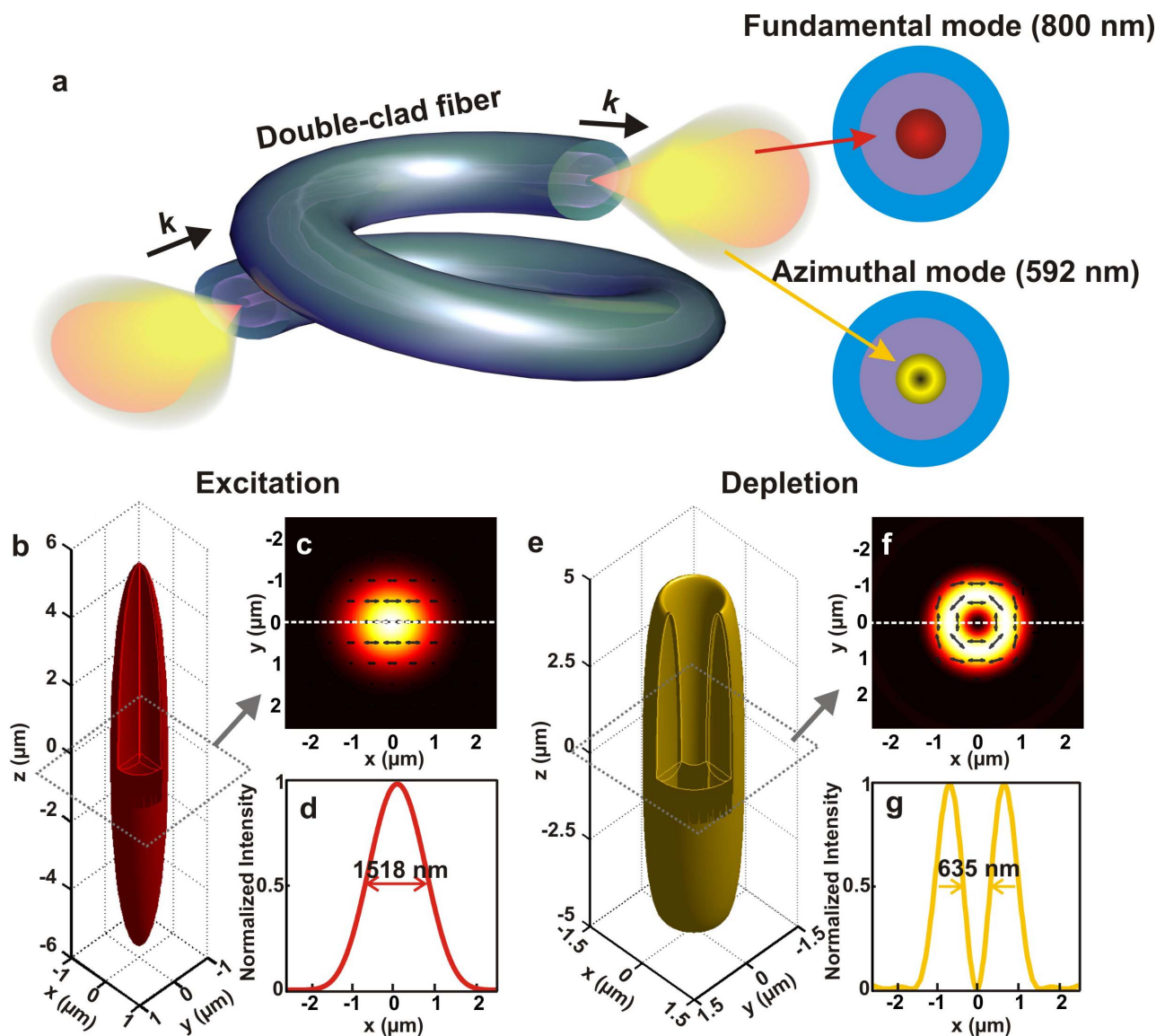
Figure 1 | Point spread function analysis for an objective with NA = 0.35. (a) Schematic of coupling both the excitation and depletion beams through the core of the double-clad fiber. (b), (c) and (d) Calculated 3D intensity distribution (point spread function), intensity distribution in the focal plane and intensity cross-section along the direction as marked in (c) for the excitation (linearly-polarized) beam at the wavelength of 800 nm. (e), (f) and (g) Calculated 3D intensity distribution (point spread function), intensity distribution in the focal plane and intensity cross-section along the direction as marked in (f) for the depletion (azimuthally-polarized) beam at the wavelength of 592 nm. The surfaces in (b) and (e) correspond to the 0.5× peak intensity. The grey square box represents the x-y plane at $z = 0$.

an efficient STED process[14–18]. In a bulky STED microscope, a circularly-polarized vortex beam is commonly used for generating a circular focal spot with the zero central intensity[19]. However, the light phase variation through optical fibers makes the maintenance of the circular polarization state at the distal end of fibers impossible. In fact, the cylindrically-polarized (azimuthally or radially polarized) beams, which can be considered as a superposition of the circularly-polarized vortex beams of opposite handedness[28–30], can be generated at the distal end of fibers by manipulating the input polarization and phase[27]. According to the diffraction theory[31] (see Methods), the focal spot of an azimuthally-polarized beam by a low NA objective is doughnut-shaped with pure transverse polarization in the focal plane (see Fig. 1), while that of a radially-polarized beam is not (see Supplementary Fig. S1).

In general, the size and the FWHM of the doughnut rings in the focal plane are determined by the topological charge n of the vortex and the polarization state of an incoming beam[19,30,32]. As shown in Fig. 1 and Supplementary Fig. S1, for both an azimuthally- and a

radially-polarized beams with topological charge 1, no doughnut-shaped focal spot can be generated. However, both an azimuthally-polarized and a radially-polarized vortex beams with topological charge 2 or higher can generate a doughnut-shaped focal spot[28,30,32]. For comparison, the size of the doughnut shape for an azimuthally-polarized beam, a circularly-polarized beam with $n = 1$, an azimuthally-polarized vortex beam with $n = 2$, and a radially-polarized vortex beam with $n = 2$ is 635 nm, 649 nm, 650 nm, and 676 nm, respectively, corresponding to the peak intensity of 0.004, 0.0032, 0.0021, and 0.0021 (normalized to the given incident power). Although, they are all suitable to achieve effective STED, an azimuthally-polarized beam is capable of generating the smallest FWHM and the highest peak intensity at the focal plane (Supplementary Figs. S2a and S2b and Supplementary Discussion), which is advantageous at the distal end of fibers for fiber-optical STED two-photon fluorescence endoscopy. In addition, the unique nature of the pure transverse polarization in the focal plane of an azimuthally-polarized beam can maximize the depletion efficiency for the given power.
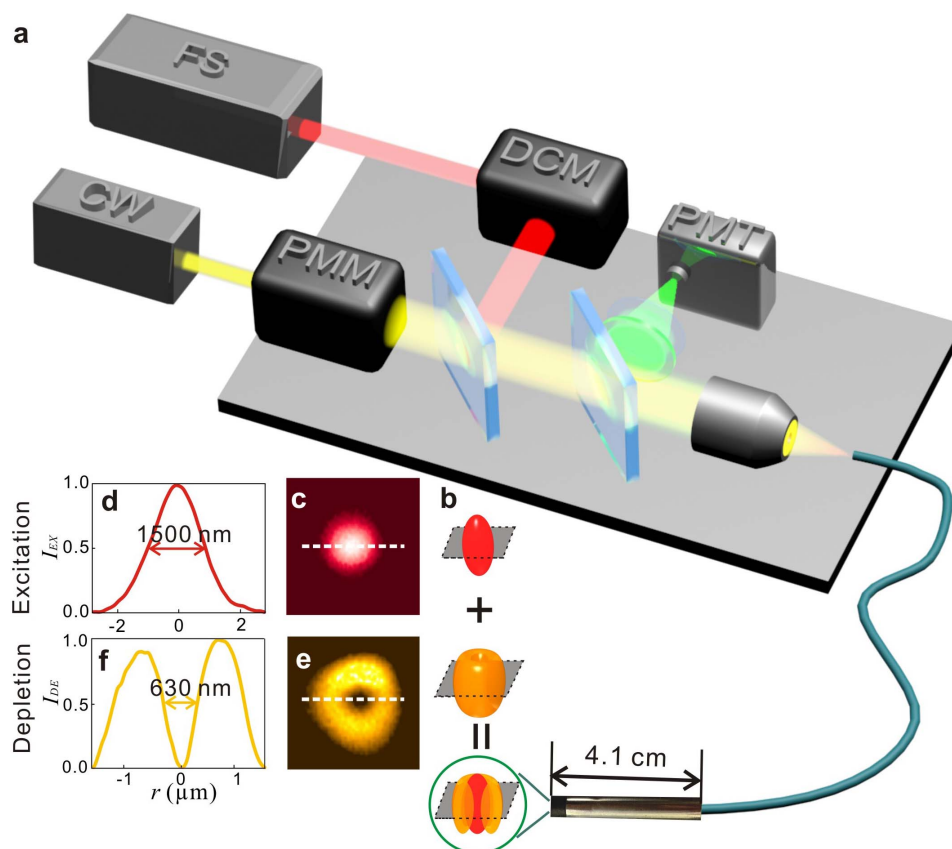
Figure 2 | Experimental setup. (a) Generation of the linearly-polarized excitation beam at the wavelength of 800 nm and the azimuthally-polarized depletion beam at the wavelength of 592 nm in a fiber-optical STED two-photon endoscope. DCM: Dispersion compensation module. PMM: Phase modulation module. PMT: Photomultiplier tube. (b) 3D plots of the focal spot achieved by the overlapping of the excitation and depletion beams in the focal region. (c) and (d): Image and cross-section of the focal spot of the excitation beam. (e) and (f): Image and cross-section of a doughnut shaped focal spot of the depletion beam. The grey squares represent the focal planes of the excitation and depletion beams.

Fiber-optical STED two-photon fluorescence endoscope. The design of the fiber-optical STED two-photon endoscope is based on the nonlinear optical endoscopy system that uses the core of a DCF (Fibercore SMM900) to deliver near infrared ultra-short optical pulses at the wavelength of 800 nm (in a fundamental mode) from a Ti:Sapphire femtosecond (FS) laser (Spectra-Physics: Mai-Tai) (Fig. 2a)[6,33,34]. To maximize the excitation efficiency, a pair of gratings is used as pre-chirp unit in the dispersion compensation module (DCM) (see Methods).

For breaking the diffraction-limited resolution barrier through the STED mechanism[14], we add a continuous wave (CW) fiber laser beam (MPB Communications Inc.) at the wavelength of 592 nm as a depletion beam (Figs. 1 and 2). Because of the cutting-off wavelength of the DCF at 900 nm, the core of the DCF can support both the fundamental mode at the wavelength of 800 nm and the higher-order mode at the wavelength of 592 nm. To convert the higher-order mode into an azimuthally-polarized beam, we adopt a phase modulation module (PMM) that comprises of a half-wave plate (HWP), a vortex phase plate (VPP) ($n = 1$) and a quarter-wave plate (QWP) to control the incident phase of the CW beam before it is coupled into the core of the DCF. Thus, focusing the beams coming from the fiber core with the micro-probe results in a Gaussian-shaped and a doughnut-shaped focal spots at wavelengths 800 nm and 592 nm (Figs. 2b–2f), as predicted by Figs. 1c and 1f. The experimental result at the wavelength of 800 nm shows that the FWHM is approximately 1500 nm (Fig. 2d), which approaches the theoretical predictions (Fig. 1d).

The intensity uniformity of the generated doughnut focal spot can be optimized by adjusting the orientations of the HWP and

the QWP, as demonstrated in Figs. 3a and 3b. It can be seen that a doughnut-shaped laser beam with an optimized intensity uniformity of approximately 86.7% can be achieved in the focal region by launching an elliptically polarized beam with topological charge of 1 (Fig. 2e), which is different from the generation of azimuthally polarized modes through a single clad optical fibers[26,27]. The FWHM of such a laser beam is approximately 630 nm (Fig. 2f), which shows good agreement with the calculated FWHM (Fig. 1g). The generation of the azimuthal polarization state is further verified experimentally (Figs. 3c–3g). To achieve the maximum depletion efficiency, the two-photon excitation process should be optimized, which is realized by the compensation for the chromatic dispersion by a pair of gratings[6] (see Supplementary Discussion), as shown in Supplementary Fig. S3.

Breaking the diffraction-limited resolution barrier. Figures 4a–4d present the fiber-optical STED two-photon endoscopic imaging of 100 nm fluorescent microspheres (Molecular Probes). As indicated in Fig. 4a, it is difficult to distinguish the two microspheres in the yellow square. However, as the depletion beam power is increased, the two microspheres are clearly separated (Figs. 4b–4d) and the FWHM of the bead images eventually reach a value of 310 nm (Fig. 4e), which breaks the diffraction-limited resolution barrier by a factor of three.

To confirm the image resolution in the fiber-optical STED two-photon endoscope, the effective intensity point spread function of the STED imaging is described as follows, which embraces two-photon excitation and one-photon depletion,
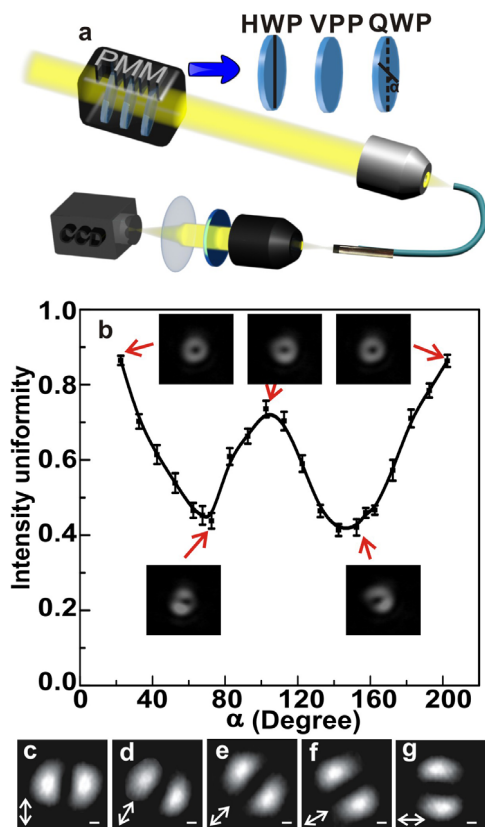
$$\left|\boldsymbol{E}_{Eff}\right|^2(x,y)=\left|\boldsymbol{E}_{Exc}\right|^4(x,y)\exp\left[-\zeta\times\left|\boldsymbol{E}_{STED}\right|^2(x,y)\times P_{STED}\right],\quad(1)$$

where $E_{Exc}(x,y)$ and $E_{STED}(x,y)$ corresponding to the excitation PSF and depletion PSF can be written as equations (9) and (2) (see Methods), respectively. ζ is the saturation factor of the depletion and is related to the material specification and P_{STED} is the power of the depletion beam in the focal region. Given the largest fluorescence depletion rate, ζ is equal to 0.064. The FWHMs of the PSF at different levels of the depletion beam power (Supplementary Fig. S4) are in good agreement with the corresponding experimental results (Fig. 4e). Fiber-optical STED two-photon fluorescence endoscopy brings a transforming future for diagnosing micro-structures *in vivo* and even conducting micro-surgery with precise control.

Discussion

Further increasing the image resolution in our system requires the higher depletion power, which may not be realistic and could lead to the damage to a sample when the depletion power is higher than 100 mW. However, a factor-of-three increase in the image resolution is an optimized result for the given microsphere sample used in this paper. To confirm this point, we theoretically reveal the fiber-optical STED two-photon fluorescence microscope with NA = 1.2 can result in the image resolution of 75 nm for the depletion power of 100 mW (Fig. 4e) due to the high peak intensity of the depletion beam (see Supplementary Figs. S2c and S2d and Supplementary Discussion), revealing an increase of the image resolution by a factor of three. Of course, if fast fluorophores with a steep depletion curve or a large depletion rate (ζ) were used, our fiber-optical STED two-photon fluorescence endoscope could result in the image resolution better than 100 nm. Alternatively, a fast scanning mechanism is capable of enhancing the depletion efficiency by avoiding the re-excitation of a fluorophore.

It should be noted that improving the axial resolution with the STED principle in the DCF endoscope system might also be possible. One of the ways is to use the superposition of a radial polarization beam with an azimuthal polarization beam in combination with a concentric π phase-shift wave plate, which can produce a 3D confinement in the focus and can be adopted for improving axial resolution[35]. The approach can be implemented in the DCF, although this process might increase the complexity of the illumination optical setup.

Figure 3 | Generation of an azimuthally-polarized beam from the core of a DCF. (a) Experimental setup for the determination of the light polarization state in the focal region. α is the angle between the fast axes of the HWP and the QWP. (b) Optimization of a doughnut azimuthally-polarized beam for the high intensity uniformity at the output end of the DCF. The insets in (b) are CCD images corresponding to α of 22.5°, 72.5°, 102.5°, 152.5° and 202.5°, respectively. The intensity uniformity of the depletion beam is defined as $\left(1-\dfrac{I_{\max}-I_{\min}}{I_{\max}+I_{\min}}\right)$, where $I_{\max}$ and $I_{\min}$ are the maximum and the minimum intensity along the doughnut ring of the azimuthally-polarized beam. (c)–(g): Characterization of the azimuthally-polarized beam in the focal region with an analyzer when it is placed at 0°, 30°, 45°, 60° and 90° with respect to the x direction. The arrows in (c)–(g) represent the direction of the analyzer. The scale bars are 470 nm.
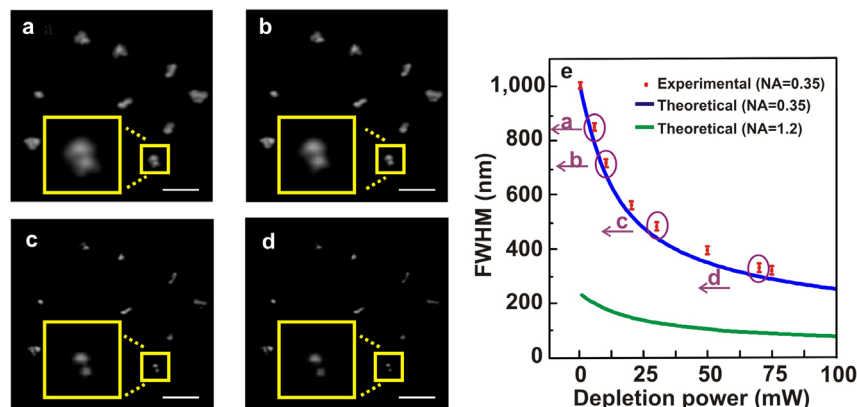

Figure 4 | Break the diffraction-limited resolution barrier. Fiber-optical STED two-photon endoscopic images of fluorescent microspheres at the power levels of 5 mW (a), 10 mW (b), 30 mW (c) and 70 mW (d), respectively. The insets are the enlarged images corresponding to the those in the yellow square. (e) The comparison of the measured and calculated FWHM values as a function of the depletion beam power for the bead images. The green curve represents the calculated FWHM values as a function of the depletion beam power for NA = 1.2 at a coverglass/water interface ($n_1/n_2 = 1.515/1.33$). The scale bars are 1.3 μm. The circled points in (e) correspond to the two-photon endoscopic images shown in (a)–(d).

4

Methods

Comparison of the doughnut focal spots. According to the diffraction theory[31], the focal spot of an objective, i.e. the point spread function (PSF) for an objective illuminated by azimuthally-polarized and radially-polarized beams can be described, respectively, as

$$E(r_2, \psi, z_2) = \frac{\pi}{\lambda}(I_x \boldsymbol{i} - iI_y \boldsymbol{j}), \tag{2}$$

where the definitions of the two variables I_x and I_y are given by

$$I_x = \int_0^\alpha P(\theta) \sin\theta \{ i^{n+1} \exp[i(n+1)\psi]J_{n+1}(kr_2\sin\theta) - i^{n-1} \tag{3}$$
$$\exp[i(n-1)\psi]J_{n-1}(kr_2\sin\theta)\} \exp(-ikz_2\cos\theta)d\theta,$$

$$I_y = \int_0^\alpha P(\theta) \sin\theta \{ i^{n+1} \exp[i(n+1)\psi]J_{n+1}(kr_2\sin\theta) + i^{n-1} \tag{4}$$
$$\exp[i(n-1)\psi]J_{n-1}(kr_2\sin\theta)\} \exp(-ikz_2\cos\theta)d\theta.$$

and

$$E(r_2, \psi, z_2) = \frac{\pi i}{4\lambda}\{ I_x \boldsymbol{i} - iI_y \boldsymbol{j} + 4I_z \boldsymbol{k} \}, \tag{5}$$

where the definitions of the three variables I_x, I_y and I_z are given by

$$I_x = \int_0^\alpha P(\theta) \sin 2\theta \{ i^{n+1} \exp[i(n+1)\psi]J_{n+1}(kr_2\sin\theta) + i^{n-1} \tag{6}$$
$$\exp[i(n-1)\psi]J_{n-1}(kr_2\sin\theta)\} \exp(-ikz_2\cos\theta)d\theta,$$

$$I_y = \int_0^\alpha P(\theta) \sin 2\theta \{ i^{n+1} \exp[i(n+1)\psi]J_{n+1}(kr_2\sin\theta) - i^{n-1} \tag{7}$$
$$\exp[i(n-1)\psi]J_{n-1}(kr_2\sin\theta)\} \exp(-ikz_2\cos\theta)d\theta,$$

$$I_z = \int_0^\alpha P(\theta) \sin^2\theta i^n \exp(in\psi)J_n(kr_2\sin\theta) \exp(-ikz_2\cos\theta)d\theta. \tag{8}$$

Here J_{n-1} and J_{n+1} are the $(n-1)^{\text{th}}$ order and the $(n+1)^{\text{th}}$ order Bessel function of the first kind, respectively. n depicts the topological charge. α is determined by the NA of an objective and can be described as $\arcsin(NA/n_1)$, where n_1 is the refractive index of the immersion medium. k is the wave vector in the medium. θ is the radial coordinate on the spherical surface of the objective. $P(\theta)$ is the sine condition of the apodization function.

A Gaussian-shaped laser beam as an excitation source can be described as

$$E(r_2, \psi, z_2) = \frac{\pi i}{\lambda}\{ [I_0 + \cos(2\psi)I_2]\boldsymbol{i} + \sin(2\psi)\boldsymbol{j} + 2iI_1\cos\psi\boldsymbol{k} \}, \tag{9}$$

where the definitions of I_0, I_1 and I_2 are given by

$$I_0 = \int_0^\alpha P(\theta)\sin\theta(1+\cos\theta)J_0(kr_2\sin\theta)\exp(-ikz_2\cos\theta)d\theta, \tag{10}$$

$$I_1 = \int_0^\alpha P(\theta)\sin^2\theta J_1(kr_2\sin\theta)\exp(-ikz_2\cos\theta)d\theta, \tag{11}$$

$$I_2 = \int_0^\alpha P(\theta)\sin\theta(1-\cos\theta)J_2(kr_2\sin\theta)\exp(-ikz_2\cos\theta)d\theta, \tag{12}$$

Through this paper, we adopt the wavelength of 800 nm for excitation and the wavelength of 592 nm for de-excitation through the STED process.

Fiber-optical two-photon fluorescence endoscope. The chromatic dispersion of the DCF which broadens the pulses is pre-chirped by a pair of gratings (400 grooves/mm, Newport) in the DCM[6]. At the distal end of the DCF, a multiple element objective (NA = 0.35) inside a small probe (diameter: 5 mm; length: 41 mm) (Fig. 2a) focuses the pulsed laser beam from the DCF to a specimen. This objective lens is designed for multi-wavelengths focusing and its chromatic aberration is well corrected and optimized[6,36,37]. The focused optical pulses excite the two-photon fluorescence signal from the specimen. The signal is collected by the inner cladding of the DCF and sent to a photomultiplier tube (PMT) after being filtered by several band-pass optical filters. A micro-scanner inside the probe scans the DCF tip in three dimensions (3D) at a real-time display rate of 0.4 mm²/s, which can achieve a field of view (FOV) of 475 μm × 475 μm with a penetration depth up to 250 μm. The PMT detection and the 3D scanning are synchronized by an electronic system, so 3D images of the specimen can be displayed and stored by a computer[6].

1. Sheppard, C. J. R. & Kompfner, R. Resonant scanning optical microscope. *Appl. Opt.* **17**, 2879–2882 (1978).

2. Denk, W., Strickler, J. H. & Webb, W. W. Two-photon laser scanning fluorescence microscopy. *Science* **248**, 73–76 (1990).

3. Sheppard, C. J. R. & Gu, M. Image formation in two-photon fluorescence microscopy. *Optik* **86**, 104–106 (1990).

4. Flusberg, B. A. *et al.* Fiber-optic fluorescence imaging. *Nat. Methods* **2**, 941–950 (2005).

5. König, K. *et al.* Clinical two-photon microendoscopy. *Micros. Res. Tech.* **70**, 398–402 (2007).

6. Bao, H., Allen, J., Pattie, R., Vance, R. & Gu, M. A fast handhold two-photon fluorescence micro-endoscope with a 475 μm × 475 μm field of view for in vivo imaging. *Opt. Lett.* **33**, 1333–1335 (2008).

7. Helmchen, F., Fee, M. S., Tank, D. W. & Denk, W. A miniature head-mounted two-photon microscope: High-resolution brain imaging in freely moving animals. *Neuron* **31**, 903–912 (2001).

8. Göbel, W., Kerr, J. N., Nimmerjahn, A. & Helmchen, F. Miniaturized two-photon microscope based on a flexible coherent fiber bundle and a gradient-index lens objective. *Opt. Lett.* **29**, 2521–2523 (2004).

9. Flusberg, B. A., Jung, J. C., Cocker, E. D., Anderson, E. P. & Schnitzer, M. J. *In vivo* brain imaging using a portable 3.9 gram two-photon fluorescence microendoscope. *Opt. Lett.* **30**, 2272–2274 (2005).

10. Fu, L., Jain, A., Xie, H., Cranfield, C. & Gu, M. Nonlinear optical endoscopy based on a double-clad photonic crystal fiber and a MEMS mirror. *Opt. Express* **14**, 1027–1032 (2006).

11. Fu, L. & Gu, M. Fibre-optic nonlinear optical microscopy and endoscopy. *J. Microsc.* **226**, 195–206 (2007).

12. Myaing, M. T., MacDonald, D. J. & Li, X. Fiber-optic scanning two-photon fluorescence endoscope. *Opt. Lett.* **31**, 1076–1078 (2006).

13. Brown, E. B. *et al. In vivo* measurement of gene expression, angiogenesis and physiological function in tumors using multiphoton laser scanning microscopy. *Nat. Medicine* **7**, 864–868 (2001).

14. Hell, S. W. & Wichmann, J. Breaking the diffraction resolution limit by stimulated emission: stimulated-emission-depletion fluorescence microscopy. *Opt. Lett.* **19**, 780–782 (1994).

15. Hell, S. W. Toward fluorescence nanoscopy. *Nat. Biotechnol.* **21**, 1347–1355 (2003).

16. Willig, K. I., Harke, B., Medda, R. & Hell, S. W. STED microscopy with continuous wave beams. *Nat. Methods* **4**, 915–918 (2007).

17. Keller, J., Schönle, A. & Hell, S. W. Efficient fluorescence inhibition patterns for RESOLFT microscopy. *Opt. Express* **15**, 3361–3371 (2007).

18. Hein, B., Willig, K. I. & Hell, S. W. Stimulated emission depletion (STED) nanoscopy of a fluorescent protein-labeled organelle inside a living cell. *PNAS* **105**, 14271–14276 (2008).

19. Zhan, Q. Properties of circuarly polarized vortex beams. *Opt. Lett.* **31**, 867–869 (2006).

20. Ganic, D., Gan, X. & Gu, M. Focusing of doughnut laser beams by a high numerical-aperture objective in free space. *Opt. Express* **11**, 2747–2752 (2003).

21. Klar, T. A., Engel, E. & Hell, S. W. Breaking Abbe's diffraction resolution limit in fluorescence microscopy with stimulated emission depletion beams of various shapes. *Phys. Rev. E* **64**, 066613 (2001).

22. Deng, S., Li, L., Li, R. & Xu, Z. STED microscopy with the azimuthally-polarized depletion beam. *Proc. of SPIE* **6826**, 682621 (2007).

23. Hao, X., Kuang, C., Wang, T. & Liu, X. Effects of polarization on the de-excitation dark focal spot in STED microscopy. *J. Opt.* **12**, 115707 (2010).

24. Khonina, S. N. & Golub, I. How low can STED go? Comparison of different write-erase beam combinations for stimulated emission depletion microscopy. *J. Opt. Soc. Am. A* **29**, 2242–2246 (2012).

25. Xue, Y., Kuang, C., Li, Shuai, Gu, Z. & Liu, X. Sharper fluorescent super-resolution spot generated by azimuthally polarized beam in STED microscopy. *Opt. Express* **20**, 17653–17666 (2012).

26. Snitzer, E. & Osterberg, H. Observed dielectric waveguide modes in the visible spectrum. *J. Opt. Soc. Am.* **51**, 499–505 (1961).

27. Volpe, G. & Petrov, D. Generation of cylindrical vector beams with few-mode fibers excited by Laguerre-Gaussian beams. *Opt. Commun.* **237**, 89–95 (2004).

28. Rao, L., Pu, J., Chen, Z. & Pu, Y. Focus shaping of cylindrically polarized vortex beams by a high numerical-aperture lens. *Opt. Laser Technol.* **41**, 241–246 (2009).

29. Lin, H. & Gu, M. Creation of diffraction-limited non-Airy multifocal arrays using a spatially shifted vortex beam. *Appl. Phys. Lett.* **102**, 084103 (2013).

30. Jiang, Y., Li, X. & Gu, M. Generation of sub-diffraction-limited pure longitudinal magnetization by the inverse Faraday effect by tightly focusing an azimuthally polarized vortex beam. *Opt. Lett.* **38**, 2957–2960 (2013).

31. Gu, M. *Advanced Optical Imaging Theory.* Springer Verlag, Heidelberg, 2000.

32. Kang, H., Jia, B. & Gu, M. Polarization characterization in the focal volume of high numerical aperture objectives. *Opt. Express* **18**, 10813–10821 (2010).

33. Gu, M., Bao, H. & Li, J. L. Cancer-cell microsurgery using nonlinear optical endomicroscopy. *J. Biomed. Opt.* **15**, 050502 (2010).

34. Gu, M., Bao, H., Gan, X., Stokes, N. & Wu, J. Tweezing and manipulating micro- and nanoparticles by optical nonlinear endoscopy. *Light: Science & Applications* **2**, doi: 10.1038/lsa.2014.7 (2014).

35. Wang, X., Ding, J., Qin, J., Chen, J., Fan, Y. & Wang, H. Configurable three-dimensional optical cage generated from cylindrical vector beams. *Opt. Commun.* **282**, 3421–3425 (2009).

36. Goets, M. *et al*. In-vivo confocal real-time mini0microscopy in animal models of human inflammatory and neoplastic diseases. *Endoscopy* **39**, 350–356 (2007).
37. Bao, H., Boussioutas, A., Reynolds, J., Russell, S. & Gu, M. Imaging of goblet cells as a marker for intestinal metaplasia of the stomach by one-photon and two-photon fluorescence endomicroscopy. *J. Biomed. Opt.* **14**, 064031 (2009).

Author contributions

Additional information